AGU PUBLICATIONS

JGR

Journal of Geophysical Research: Space Physics

RESEARCH ARTICLE
10.1002/2014JA020365

Key Points:
- A 3-D MHD simulation of CME evolution in a realistic solar wind is presented
- Real 3-D nature of CME in morphology and their evolution is reproduced well
- A satisfactory comparison with the in situ plasma data from Wind is provided

Correspondence to:
F. Shen,
fshen@spaceweather.ac.cn

Citation:
Shen, F., C. Shen, J. Zhang, P. Hess, Y. Wang, X. Feng, H. Cheng, and Y. Yang (2014), Evolution of the 12 July 2012 CME from the Sun to the Earth: Data-constrained three-dimensional MHD simulations, *J. Geophys. Res. Space Physics*, *119*, 7128–7141, doi:10.1002/2014JA020365.

Received 8 JUL 2014
Accepted 5 SEP 2014
Accepted article online 8 SEP 2014
Published online 26 SEP 2014

Evolution of the 12 July 2012 CME from the Sun to the Earth: Data-constrained three-dimensional MHD simulations

Fang Shen[1], Chenglong Shen[2], Jie Zhang[3], Phillip Hess[3], Yuming Wang[2], Xueshang Feng[1], Hongze Cheng[2], and Yi Yang[1]

[1]SIGMA Weather Group, State Key Laboratory of Space Weather, Center for Space Science and Applied Research, Chinese Academy of Sciences, Beijing, China, [2]School of Earth and Space Sciences, University of Science and Technology of China, Hefei, China, [3]School of Physics, Astronomy, and Computational Sciences, George Mason University, Fairfax, Virginia, USA

Abstract The dynamic process of coronal mass ejections (CMEs) in the heliosphere provides us the key information for evaluating CMEs' geoeffectiveness and improving the accurate prediction of CME-induced shock arrival time at the Earth. We present a data-constrained three-dimensional (3-D) magnetohydrodynamic (MHD) simulation of the evolution of the CME in a realistic ambient solar wind for the 12–16 July 2012 event by using the 3-D corona interplanetary total variation diminishing (COIN-TVD) MHD code. A detailed comparison of the kinematic evolution of the CME between the observations and the simulation is carried out, including the usage of the time elongation maps from the perspectives of both STEREO A and STEREO B. In this case study, we find that our 3-D COIN-TVD MHD model, with the magnetized plasma blob as the driver, is able to reproduce relatively well the real 3-D nature of the CME in morphology and their evolution from the Sun to the Earth. The simulation also provides a relatively satisfactory comparison with the in situ plasma data from the Wind spacecraft.

1. Introduction

Coronal mass ejections (CMEs) are a large-scale eruption of magnetized plasma from the Sun's corona and subsequently propagate into interplanetary space. They are the main drivers of space weather near the Earth, accounting for about 85% of intense geomagnetic storms [*Zhang et al*., 2007], especially when they contain organized southward directed magnetic fields. However, not all of CMEs originating from the vicinity of solar center can encounter the Earth [e.g., *Wang et al*., 2002; *Yermolaev and Yermolaev*, 2006; *Shen et al*., 2014, and references therein]. Therefore, it is of great importance to understand how they propagate and evolve in interplanetary space and how their properties as observed at 1 AU are related to the properties observed near the Sun [e.g., *Lugaz et al*., 2011].

In recent years, numerical simulations of interplanetary coronal mass ejections (ICMEs) have become one of the primary tools to investigate the propagation of ICMEs and their interaction with the interplanetary medium. The in-depth study of the evolution of CMEs in the heliosphere heavily depends upon numerical models. There have been Sun-to-Earth numerical simulations of real events [e.g., *Chané et al*., 2008; *Lugaz et al*., 2007, 2011; *Tóth et al*., 2007; *Shen et al*., 2007, 2011a, 2011b]. Particular attention has been given to the numerical modeling of CMEs at or near solar minimum, especially the 12 May 1997 CME [*Odstrcil et al*., 2004; *Wu et al*., 2007; *Cohen et al*., 2008; *Titov et al*., 2008; *Zhou et al*., 2008]. One reason for such choice is that the ambient solar wind is believed to be simpler and steadier during solar minimum, thus easier to modeling, than that during the solar maximum. Therefore, solar minimum is thought to be the perfect period to study the evolution of CMEs. Meanwhile, there still exist a few numerical works of CME events at or near solar maximum, e.g., the 4 April 2000 CME [*Chané et al*., 2008; *Shen et al*., 2011a].

However, not all of these previous works have been totally successful in reproducing the observed transit time and the measured plasma properties at 1 AU, especially for the CMEs near the maximum. One of the possible reasons is that some parameters, particularly the initial speeds, of CMEs for those events are not well constrained, because Earth-directed CMEs appearing halo suffer from the projection effect, and there were no direct observations then between 32 R_s and the Earth. With the launch of the twin Solar Terrestrial Relations Observatory (STEREO) spacecraft in 2006 [*Kaiser et al*., 2008], CMEs can be imaged continuously

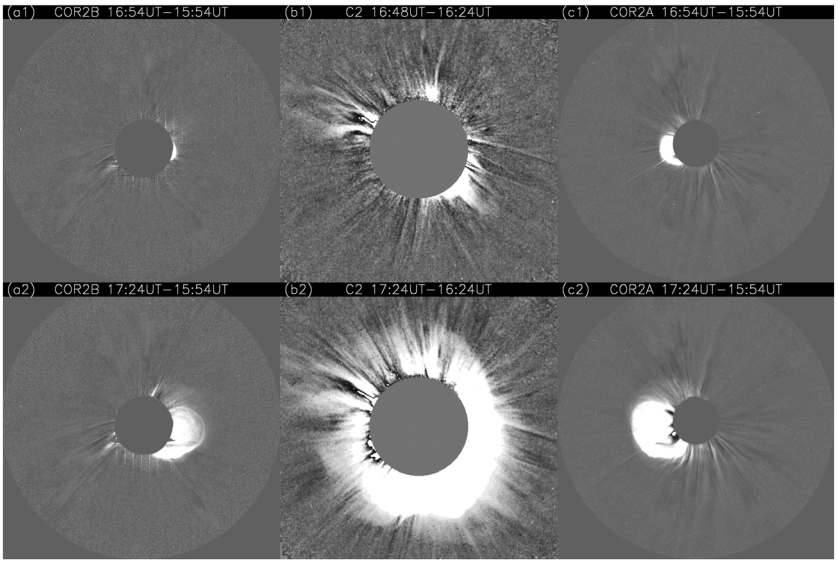

Figure 1. Running difference images at (top) 16:54 UT and (bottom) 17:24 UT on 12 July 2012 from (left) STEREO A COR2, (right) STEREO B COR2, and (middle) SOHO/LASCO C2, respectively.

from the solar surface to 1 AU with coronagraphic and heliospheric imagers onboard STEREO [*Howard et al.*, 2008]. This provides the opportunity to directly compare the simulation results with the observations continuously in time and space. We believe that constructing a data-constrained numerical model is necessary to reproduce the measured plasma properties at 1 AU, in which both the imaging data and the in situ data should be used to constrain the initial parameters of the CME, including propagation direction, speed, density, temperature, and magnetic field.

In this article, we study the kinetic evolution of the 12–16 July 2012 CME event. The event was recently studied by several authors using observational or theoretical method [*Möstl et al.*, 2014; *Cheng et al.*, 2014; *Dudík et al.*, 2014; *Hess and Zhang*, 2014]. Thus, it is intriguing to study the 12–16 July 2012 CME event using the data-constrained 3-D magnetohydrodynamic (MHD) numerical method and compare the simulated Sun-to-Earth evolution results with the actual observations in 3-D space and continuously in time. The organization of the paper is as follows: We describe the observations and numerical models in section 2. Details of the kinematic evolution of the CME in interplanetary space are discussed in section 3. This section also includes the synthetic STEREO-like line-of-sight images and the comparison of the time elongation maps (*J* maps) between synthetic results and white-light observations. The comparison with the in situ data at 1 AU is also explored. In the last section, summary and discussion are given.

2. Observations and Methods

The event on 12–16 July 2012 is a fast, Earth-directed CME occurring at the solar maximum in the 24th solar cycle and belonging to Carrington Rotation (CR) 2125, with an initial speed of 1531 km/s at 2 R_s and initial direction of S09W01 [*Hess and Zhang*, 2014]. Over 14 and 15 July 2012 and through the early time of 16 July, the Earth experienced a strong geomagnetic storm with peak *Dst* of −127 nT, which created an aurora visible at lower latitudes of the Earth. This event was very well observed and tracked by the imaging instruments on STEREO due to the optimal propagation direction of the CME and the viewing angles of STEREO A and STEREO B.

2.1. The Solar Eruption of 12 July 2012

The CME of interest originated from active region (AR) 11520. The active region first appeared on the solar disk from the eastern limb on about 5 July 2012 and rotated beyond the western limb on about 19 July 2012. During this period, this active region produced seven *M* class flares and one *X* class flare. The *X*1.4 class flare occurred at 15:37 UT on 12 July, which was accompanied by the CME we study in this work. This AR also produced another full halo CME on 19 July 2012, one partial halo CME on 17 July 2012, and the 23 July 2012 extreme space weather event [*Ngwira et al.*, 2013; *Russell et al.*, 2013; *Baker et al.*, 2013].

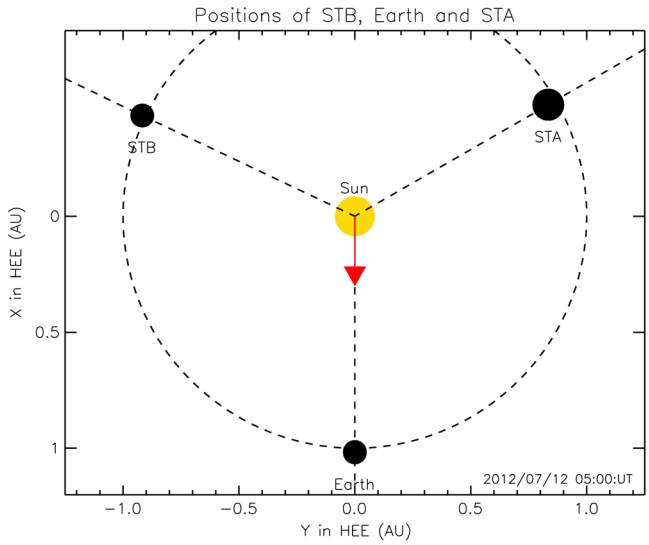

Figure 2. The positions of STEREO A (STA) and STEREO B (STB) in the HEE coordinates on 12 July 2012.

The full halo CME of interest was first seen in the Large Angle and Spectrometric Coronagraph (LASCO) C2 field of view on 12 July 2012 at 16:48 UT. Figure 1 shows the running difference coronagraph images at 16:54 UT and 17:24 on 12 July 2012 from STEREO A (STA) COR2, STEREO B (STB) COR2, and SOHO/LASCO C2. The positions of STA and STB in Heliocentric Earth Ecliptic (HEE) coordinates on 12 July 2012 are illustrated in Figure 2.

The projected linear speed, according to the Coordinated Data Analysis Workshop LASCO CME catalog, is 885 km/s. The *X*1.4 flare peaked at 16:49 UT with the location at the heliographic coordinate S13W15. Using STEREO observations and the graduated cylindrical shell (GCS) model to reconstruct and measure the 3-D CME [*Thernisien et al*., 2006, 2009], we determined that the propagation direction of the CME is S09W01, which was almost pointing to the Earth. The CME reached 5 R_s from the Sun center at 16:55 UT at a true speed of 1494 km/s [*Hess and Zhang*, 2014] as determined by fitting the height measurements from the GCS model.

About 2 days later, this CME arrived on Earth, and a strong shock was recorded by the Wind spacecraft on 14 July at 17:00 UT. The interplanetary disturbance caused by this event, the CME-driven shock, took about 48 h and 12 min to reach the Earth.

2.2. Three-Dimensional MHD Model and Simulation Method

In this section, the 3-D MHD simulation of the background solar wind for Carrington Rotation (CR) 2125 is presented. The computational domain here covers 1 $R_s \le r \le 220$ R_s, $-89° \le \theta \le 89°$, and $0° \le \varphi \le 360°$, where r is the radial distance from solar center in units of solar radius R_s and θ and φ are the elevation and azimuthal angles, respectively. The grid mesh is chosen to be $464(r) \times 89(\theta) \times 180(\varphi)$. The grid size is uniform in azimuth, with $\Delta\varphi = 2°$. The radial grid (r_i) and meridional grid (θ_j) are not uniform. In order to obtain a precise computational resolution, we choose for the radial grid: $r(1) = 1.0$ R_s, $\Delta r(1) = s \times r(1)$, $r(i) = r(i-1) + \Delta r(i-1)$, and $\Delta r(i) = s \times r(i-1)$, where $s = \pi/225$ ($\pi = 3.1415926$) between 1 R_s and 23 R_s and $s = \pi/315$ between 23 R_s and 220 R_s. The spatial resolution in the radial direction gradually varies from ~0.01 R_s at the inner boundary of 1 R_s to ~2.0 R_s near 1 AU. For the meridional grid, we choose $\Delta\theta$ (0°) = 1.0°, $\Delta\theta$ (−89°) = $\Delta\theta$ (89°) = 3.0°, with a constant increase in $\Delta\theta$ from $\theta = 0°$ to $\theta = \pm 89°$.

The numerical scheme we used is a 3-D corona interplanetary total variation diminishing (COIN-TVD) scheme in a Sun-centered spherical coordinate system (r, θ, φ) [*Feng et al*., 2003, 2005; *Shen et al*., 2007, 2009]. The time-dependent 3-D ideal MHD equations used in this study include solar rotation [e.g., *Shen et al*., 2007] and heating source term [*Feng et al*., 2010; *Zhou et al*., 2012], where the pressure equation and the volumetric heating function S_E are given by

$$\frac{\partial p}{\partial t} + \frac{1}{r^2}\frac{\partial r^2(pv_r)}{\partial r} + \frac{1}{r\sin\theta}\frac{\partial \sin\theta(pv_\theta)}{\partial \theta} + \frac{1}{r\sin\theta}\frac{\partial (pv_\varphi)}{\partial \varphi} = -(\gamma-1)p\nabla\cdot\vec{v} + (\gamma-1)S_E$$

where S_E is the heating source term, with the form of $S_E = Q\exp[-r/L_Q]$, which is defined by following the work of *Nakamizo et al*. [2009], *Feng et al*. [2010, 2011], and *Zhou et al*. [2012]. Q and L_Q are the intensity and decay length of heating, respectively. The heating intensity is defined as $Q = Q_0/f_s$. In this research, L_Q and the constant value of Q_0 are set to be 0.9 R_s and 1.0×10^{-6} J m^{-3} s^{-1}, respectively. The expansion factor f_s is defined as $f_S = \left(\frac{R_s}{r}\right)^2 \frac{B_{Rs}}{B_r}$, where R_s and r are 1 R_s and the distance from the solar center and B_{Rs} and B_r are the

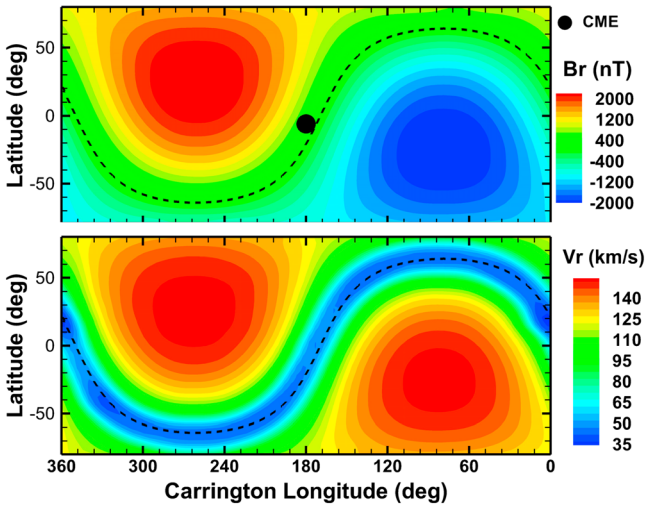

Figure 3. The steady state distribution of radial component of (top) magnetic field and (bottom) velocity at 5 R_s. The dashed lines in each panel show the location of $B_r = 0$.

magnetic field strength at the solar surface and at *r*. In this simulation, the expansion factor is time invariant and the same as the value we used during calculating the background solar wind. The involvement of expansion factor in the heating source term is encouraged by the fact that the solar wind speed is inversely correlated with the expansion rate of the magnetic flux tube in the corona [*Levine et al.*, 1977]. Here we follow the work by *Rempel et al.* [2009] to calculate the diffusion flux $f_{i+\frac{1}{2}}$ by using the extrapolated values at the cell interface $u_l = u_i + 0.5\ \Delta u_i$ and $u_r = u_{i+1} - 0.5\ \Delta u_{i+1}$: $f_{i+\frac{1}{2}} = \frac{1}{2} c_{i+\frac{1}{2}}(u_r - u_l)$, where Δu_i is limited by the slope limiter minmod to make the numerical scheme TVD, as shown following [*Feng et al.*, 2003]

$$\Delta u_i = \min \mathrm{mod}\left(\delta u_{i-1/2},\ \delta u_{i+1/2}\right),\ \delta u_{i+1/2} = u_{i+1} - u_i,\ \delta u_{i-1/2} = u_i - u_{i-1},$$

Here $\mathrm{minmod}(x, y) = \mathrm{sgn}(x)\mathrm{Max}\ (0, \min[|x|, y\mathrm{sgn}(x)])$, where $\mathrm{sgn}(x) = \begin{cases} 1, & x > 0; \\ 0, & x = 0; \\ -1, & x < 0. \end{cases}$

The characteristic velocity c is defined as $c = 0.1\ c_{\mathrm{sound}} + v + v_{\mathrm{alf}}$, which significantly reduces the diffusivity in low Mach number flows. This scheme has been applied to all MHD variables and accounts for the effects of mass diffusion in the momentum and pressure fluxes. The $\nabla \cdot \vec{B}$ error produced by the diffusion scheme is controlled by iterating

$$\vec{B}^{\,n+1} - \vec{B}^{\,n} = \mu(\Delta x)^2 \mathrm{grad}\left(\mathrm{div}\vec{B}^{\,n}\right),$$

where n is the number of iteration and $(\Delta x)^2 = \frac{3}{\frac{1}{(\Delta r)^2} + \frac{1}{(r\Delta\theta)^2} + \frac{1}{(r\sin\theta\Delta\varphi)^2}}$ is in the spherical coordinate system. The value μ is set as 0.35 to satisfy $\max\left(\frac{\Delta x|\nabla\cdot\vec{B}|}{|\vec{B}|}\right) < 10^{-3}$ in less than 50 iterations ($n < 50$). This artificial diffusivity can lead to a scheme that is fully shock capturing, at least second-order accuracy in smooth regions (higher order is possible depending on the slope limiter used) [*Rempel et al.*, 2009; *van der Holst and Keppens*, 2007; *Feng et al.*, 2011].

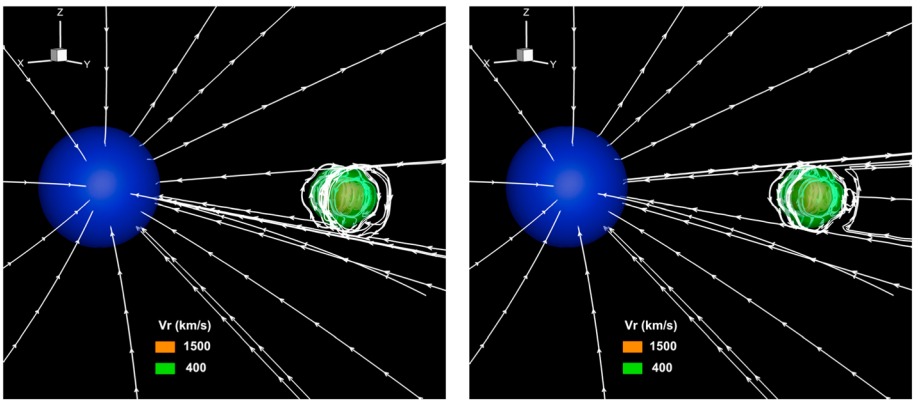

Figure 4. Three-dimensional views of the CME initialization including two levels of isosurfaces of the radial velocity and the magnetic field lines with (a) $\Psi_0 = -4.0$ and (b) $\Psi_0 = 4.0$.

Table 1. Initial Parameters of the CME

	D	v_{ave} km/s	$n_{ave} \times 10^7$ cm^{-3}	$T_{ave} \times 10^6$ K	Ψ_0	a_{CME} R_s	$B_{ave} \times 10^5$ nT	Mass $\times 10^{12}$ kg	Momentum $\times 10^{15}$ kg km s^{-1}
CME	S09W01	1494	2.0	6.0	−4.0	0.6	6.0	2.45	3.67

At the inner boundary (1 R_s), the method of projected characteristics [*Wu and Wang*, 1987; *Hayashi*, 2005; *Wu et al*., 2006] is employed. At the outer boundary of $r = 220$ R_s, and the boundaries at −89° and 89°, we employ a linear extrapolation. The detailed description of the asynchronous and parallel time-marching method for the 3-D MHD simulation is discussed in detail by *Shen et al*. [2007, 2009, 2011a, 2011b].

We first establish a steady state background solar wind. The potential field, extrapolated from the observed line-of-sight magnetic field of CR 2125 on the photosphere from the Wilcox Solar Observatory (WSO), and Parker's solar wind solution are used as the initial magnetic field and velocity. The initial density is deduced from the momentum conservation law, and the initial temperature is given by assuming an adiabatic process. With these initial conditions, our MHD code may quickly reach a self-consistent steady state of solar wind.

Figure 3 shows the steady state distribution of radial component of magnetic field and velocity at 5 R_s. The location of $B_r = 0$ is indicated by the dashed lines. Figure 3 indicates that the corona current sheet becomes nearly vertical to the ecliptic plane, which is rather typical at the solar maximum. From Figure 3 (bottom), it could also be found that the distribution of the low-speed region is basically consistent with the corona current sheet region.

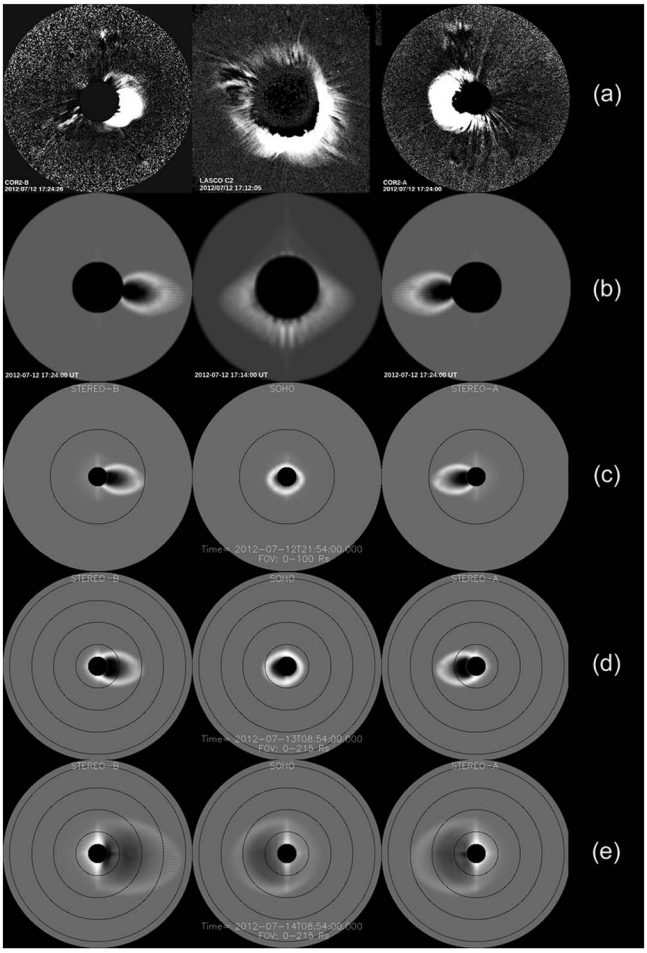

Figure 5. Comparison of (a) real and (b) synthetic (left) STEREO/COR2B, (right) STEREO/COR2A, and (middle) LASCO/C2 images at 17:24 UT on 12 July. Synthetic images at (c) 21:54 UT on 12 July, at (d) 08:54 UT on 13 July, and at (e) 08:54 UT on 14 July.

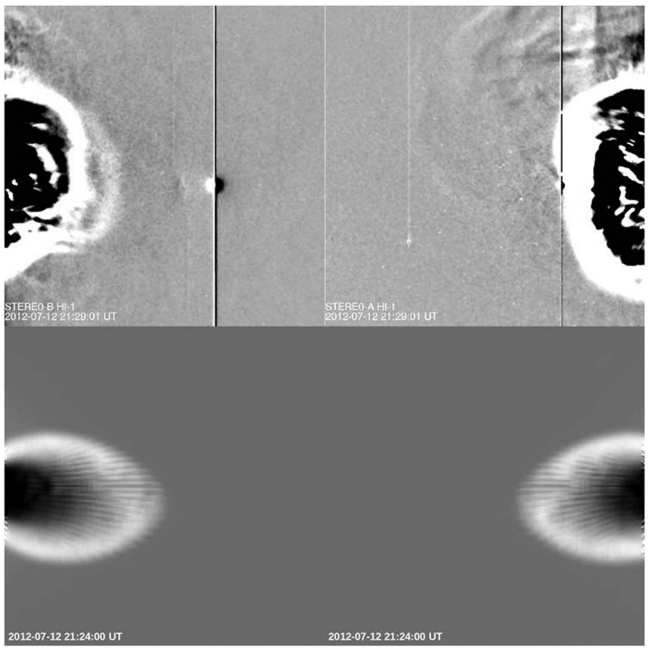

Figure 6. Comparison of (top) real and (bottom) synthetic (left) SECCHI/HI-1B and (right) SECCHI/HI-1A images at 21:29 UT on 12 July.

The CME is modeled as a magnetic blob with its center sitting at $r = 5\ R_s$, just as we did in the previous work [*Chané et al.*, 2005; *Shen et al.*, 2011a, 2013]. To reproduce the evolution of the 12 July 2012 event, the initial propagation direction and velocity are chosen to be the same as those determined from the observations. From the observations, the direction of the CME is S09W01, and the propagation speed at 5 R_s is 1494 km/s. Thus, the average speed of the plasma blob (v_{ave}) is set to be 1494 km/s, and the maximum velocity inside the plasma blob should be ~3 v_{ave} [*Chané et al.*, 2005; *Shen et al.*, 2011a].

The density, radial velocity, and temperature profile of the initial perturbation are defined as follows:

$$\begin{cases} \rho_{CME}(r,\theta,\varphi) = \dfrac{\rho_{max}}{2}\left(1 - \cos\left(\pi\dfrac{a_{CME} - a(r,\theta,\varphi)}{a_{CME}}\right)\right) \\ V_{CME}(r,\theta,\varphi) = \dfrac{v_{max}}{2}\left(1 - \cos\left(\pi\dfrac{a_{CME} - a(r,\theta,\varphi)}{a_{CME}}\right)\right) \\ T_{CME}(r,\theta,\varphi) = \dfrac{T_{max}}{2}\left(1 - \cos\left(\pi\dfrac{a_{CME} - a(r,\theta,\varphi)}{a_{CME}}\right)\right) \end{cases}$$

where a_{CME} is the radius of the initial plasma blob; $a(r, \theta, \varphi)$ denotes the distance from the center of the initial plasma blob; and ρ_{max}, v_{max}, and T_{max} are the maximum density, radial velocity, and temperature in the plasma bubble added on top of the background solar wind, respectively.

The initial magnetic field of the perturbation in r and θ direction can be defined as [*Shen et al.*, 2011a, 2011b]

$$\begin{cases} B_{r_{CME}}(r,\theta,\varphi) = -\dfrac{1}{r^2\sin\theta}\dfrac{\partial\psi(r,\theta,\varphi)}{\partial\theta} \\ B_{\theta_{CME}}(r,\theta,\varphi) = \dfrac{1}{r\sin\theta}\dfrac{\partial\psi(r,\theta,\varphi)}{\partial r} \end{cases}$$

where

$$\psi(r,\theta,\varphi) = \psi_0\left(a(r,\theta,\varphi) - \frac{a_{CME}}{2\pi}\sin\left(\frac{2\pi a(r,\theta,\varphi)}{a_{CME}}\right)\right)$$

is the magnetic flux function. Ψ_0 is the constant, and different sign of Ψ_0 denotes different polarity of the magnetized plasma blob [*Chané et al.*, 2006]. The two panels of Figure 4 give the 3-D views of the CME initialization, showing the isosurfaces of radial velocity (v_r) and the magnetic field lines by using different Ψ_0 of −4.0 (Figure 4a) and 4.0 (Figure 4b). It could be found that the polarity of the initial CMEs in Figures 4a and 4b is opposite.

Table 1 lists the initial parameters of the CME from the observations. The choice of other parameters is given to match the transit time of the shock, the total magnetic field, and other Wind data at the shock as the best fit as possible. Therefore, all the initial parameters of the CME are constrained by observations. The input of the mass and the momentum of the CME are 2.45×10^{12} kg and 3.67×10^{15} kg km s^{-1}, respectively. The relative pressure, which is defined as $(P_{CME} - P_{bg}) / P_{bg}$, is about 0.32, where P_{CME} and P_{bg} are the pressures of CME and local background solar wind, respectively.

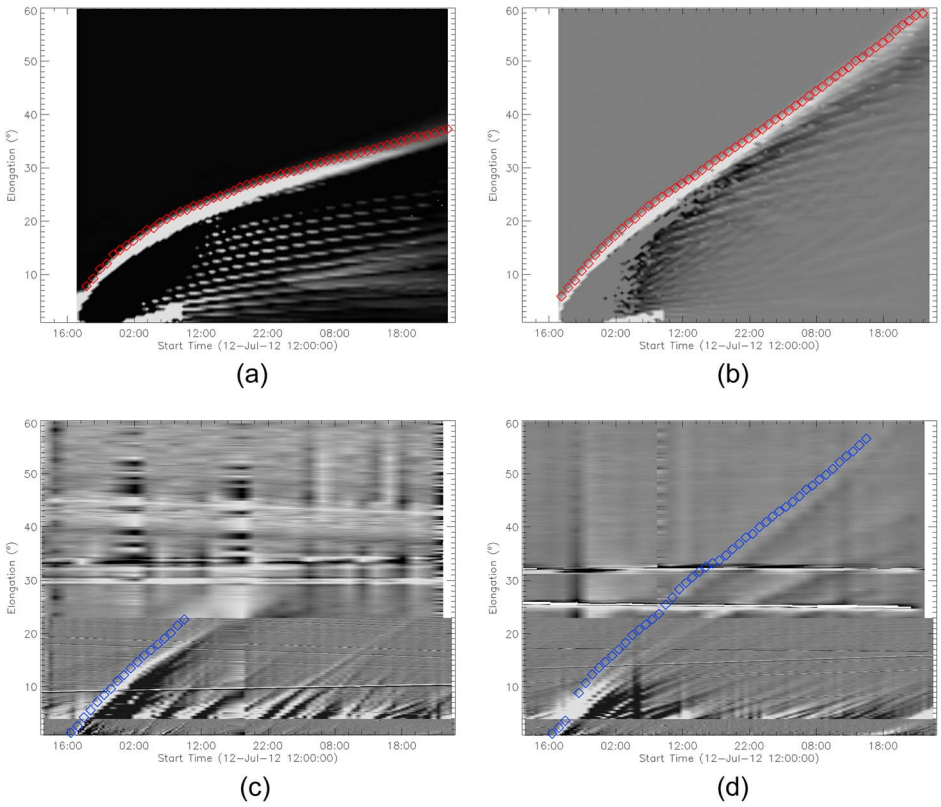

Figure 7. (a and b) Synthetic *J* maps corresponding to the position of STA and STB. (c and d) Real *J* maps constructed based on the imaging data from COR2, HI-1, and HI-2 imagers onboard STA and STB.

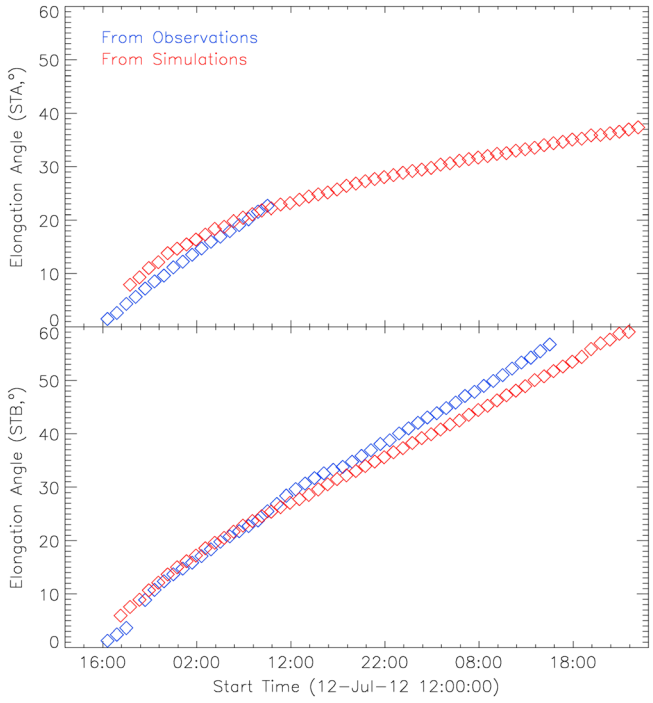

Figure 8. Comparison between time elongation profiles from the observations (blue diamond) and the synthetic images derived from simulation (red diamond) corresponding to the position of (top) STA and (bottom) STB.

3. Kinematic Evolution of the CME

3.1. Comparisons With Coronagraph Images

Detailed studies of synthetic line of sight images from modeling have been performed by a number of groups in the past [*Chen and Krall*, 2003; *Manchester et al.*, 2004; *Lugaz et al.*, 2005, 2009; *Odstrcil et al.*, 2005; *Riley et al.*, 2008]. The direct comparison of such synthetic observations with real observations has only been done in recent years for a few selected events during or close to the solar maximum [*Lugaz et al.*, 2007, 2009; *Manchester et al.*, 2008; *Sun et al.*, 2008].

Synthetic coronagraph images of CMEs seem to be a simple and relevant way to display 2-D (two-dimensional) representations of simulated CMEs [*Lugaz et al.*, 2009]. Line-of-sight images are the best way to study the density structure of CMEs. Producing synthetic white-light images and comparing

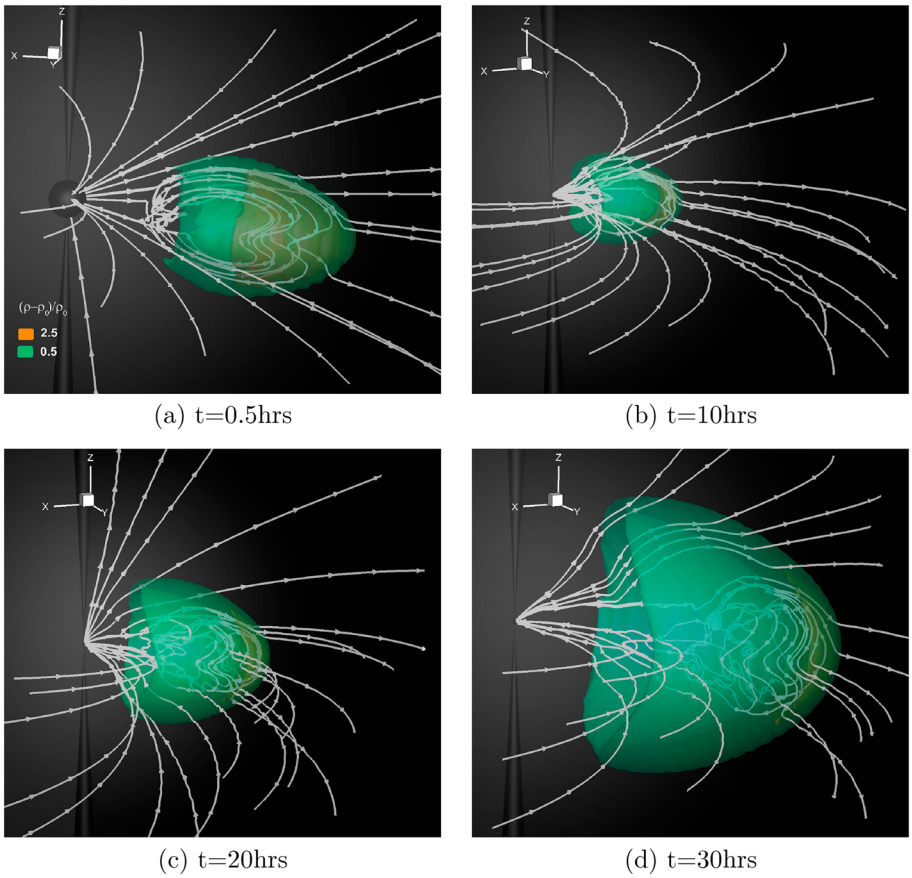

Figure 9. Three-dimensional view of the relative density ($(\rho - \rho_0)/\rho_0$) distribution at $t = 0.5$, 10, 20, and 30 h. The color code in the panels represents the two levels of isosurfaces of the relative density. The magnetic field topology is represented by the white magnetic field lines.

those with 3-D data sets will provide information on how the density structure of a CME obtained from real coronagraphs is related to the 3-D structure of the CME [*Lugaz et al.*, 2007].

To turn the 3-D simulation into an image comparable to remote sensing images, the approximate position of the desired view (SOHO, STEREO A, and STEREO B) must be determined in a heliocentric coordinate system. The positions of STA and STB in the HEE coordinates at 12 July 2012 are plotted in Figure 2. At that time, STA is separated away from the Earth by about 120° at a radial distance of 0.96 AU from the Sun and STB by about 115° at a radial distance of 1.01 AU from the Sun. The total field of view must also be specified, in terms of an angular extent. For instance, the field of view on the STEREO COR2 instrument is approximately 2–15 R_s, or in terms of angular field of view, approximately 0.5–4° from the solar center. For each pixel in the computation domain, its angular position relative to the observer is calculated. If the pixel is within the angular limits of the image cone, it is projected onto the plane of sky, and the image coordinates of the pixel are calculated. The value of the relative density of the computational pixel is then added into the image pixel. This calculation is carried out over each pixel in the grid, and the sums are compiled for the each image pixel so that a complete image can be assembled.

Figure 5a shows remote sensing observations from STEREO COR2B, COR2A, and SOHO/LASCO C2 at 17:24 UT on 12 July. Figures 5b to 5e show the synthetic images from simulation at 17:24 UT (Figure 5b) and 21:54 UT (Figure 5c) on 12 July, at 08:54 UT (Figure 5d) on 13 July, and at 08:54 UT (Figure 5e) on 14 July, respectively. The synthetic images are produced based on the relative density data from the 3-D simulation output. Figure 6 shows the comparison of real and synthetic Sun Earth Connection Coronal and Heliospheric Investigation (SECCHI)/HI-1B (Figure 6, left) and SECCHI/HI-1A (Figure 6, right) images at 21:29 UT on 12 July. There is a fair agreement of the overall shape and the propagation direction of the CME between

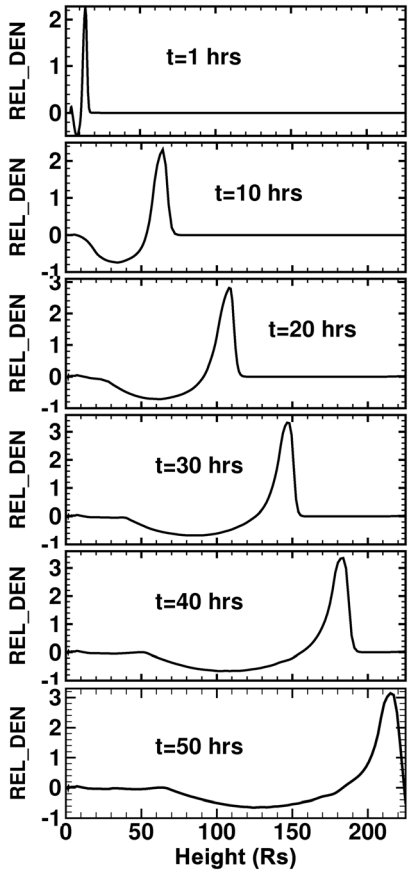

Figure 10. Evolution of the relative density $((\rho - \rho_0)/\rho_0)$ versus heliocentric distance from 0 to 225 R_s along the Sun-Earth line ($\theta = 0°$ and $\varphi = 180°$) at (top to bottom) $t = 1$, 10, 20, 30, 40, and 50 h, respectively.

observations and simulations. However, the CME leading edge in the synthetic images moves slightly more ahead than that in the real coronagraph images. This might be due to the adopted CME blob, since the unrealistic initiation mechanism is challenging unclear. The CME model does not include the expansion speed at its initialization. Therefore, at the early stage, the simulated CME propagates a bit faster than the observations in *r* direction, while in the direction perpendicular to *r* direction, the expansion of the simulated CME is quite smaller than that of the observations.

3.2. Comparisons With Time Elongation Maps (*J* Maps) and Kinetic Evolution of the Shock

The comparison between synthetic numerical results and real white-light observations in section 3.1 is mainly for the CME morphology at very early stages. The following comparison is for the CME kinematics from near the Sun to 1 AU. One of the methods to track the CME in interplanetary space is to produce time elongation maps (*J* maps) [e.g., *Sheeley et al*., 1997, 2008; *Rouillard et al*., 2008; *Davies et al*., 2009]. *J* maps allow for the tracking of CMEs to large elongation angles and enable the study of their evolution without concerning the direction of propagation.

Here we study the *J* maps along the Sun-Earth line. Considering the Thomson scatter [*Jackson*, 1997], we translate the simulated density distribution in the ecliptic plane to the brightness distribution. Then, a slice is obtained by showing the total brightness along the elongation angles from 1° to 80°. To get the synthetic *J* map, we take a total brightness of the slice every 30 min and plot the running difference results. For the real *J* map, a slice is taken for every observational image, and the running difference is plotted.

Figures 7a and 7b give the synthetic *J* maps corresponding to the position of STA and STB, respectively. Figures 7c and 7d show the real *J* maps constructed from the imaging data from COR2, HI-1, and HI-2 imagers onboard STA and STB by placing a slice along the ecliptic plane. Every stripe in a *J* map indicates a featured element moving away from near the Sun to 1 AU. In order to compare the stripes of the CME feature between the synthetic *J* maps and real *J* maps, we track and locate the CME's leading edge in the synthetic *J* maps by red diamonds (Figures 7a and 7b) and in the real *J* maps by blue diamonds (Figures 7c and 7d). The real *J* map at the STA is much more complicated and harder to recognize at large elongation, so we only mark the CME's leading edge in the region with elongation less than 23°, as shown in Figure 7c. Then, we make the quantitative comparison between synthetic numerical results and real white-light observations from the *J* maps. Figure 8 plots the time elongation profiles from the observations (blue diamond) and the synthetic images derived from simulation (red diamond) corresponding to the position of STA and STB. This comparison shows that the simulation offers a satisfactory reproduction of the observations, except at very early stage, e.g., before 22:00 UT on 12 July.

The time of introducing CME into the computational domain is set to be zero. We locate the CME by simply setting a threshold of 0.5 in the map of relative density $(\rho - \rho_0)/\rho_0$, where ρ is the total density and ρ_0 is the density of the background solar wind. Figures 9a to 9d show the 3-D view of the relative density and magnetic field distribution at $t = 0.5$, 10, 20, and 30 h. The color code in the panels represents the two levels of isosurfaces of the relative density. And the outer isosurface with the relative density of 0.5 mainly denotes the shock surface of the CME. The magnetic field topology in Figure 9 is represented by white magnetic field lines. A CME leading edge with a high density is clearly visible in front of the flux rope. At the early time of 0.5 h,

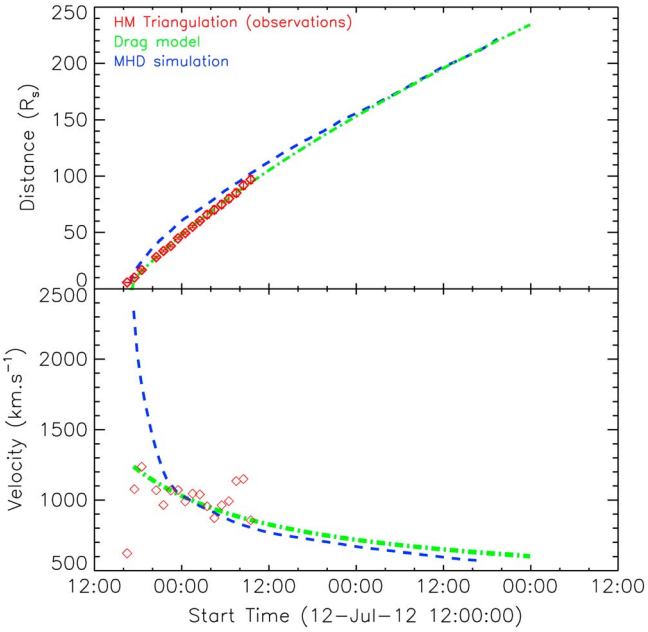

Figure 11. Time-height plot and the time-speed plot of the shock from near the Sun to the Earth. The blue dashed lines, the green dash-dotted lines, and the red diamonds indicate the time-height and the time-speed distributions of the shock front from the simulation, from the shock drag model based on the observations, and from the HM triangulation method based on the observations.

because the initial radial velocity of CME is much larger than the background solar wind speed, the shape of the CME looks like an "olive." As the CME propagates into the heliosphere, it expands obviously in the direction perpendicular to the propagation direction, and it is radially compressed.

Next, we focus on the quantitative comparison of the time-heliosdistance and the time-speed on the shock front between the 3-D numerical results and the observations. Figure 10 shows the evolution of the relative density $((\rho - \rho_0)/\rho_0)$—distance profile along the Sun-Earth line at six consecutive times, in which we could recognize that the leading edge of the CME is located near the position of CME density peak. At the very early time of $t = 1$ h, the relative density profile has an obvious sharp jump from ~11 R_s to ~16 R_s. As time goes, the width of the relative density jump along the Sun-Earth line increases apparently. At 10 h, the width of the jump is near 18 R_s; at 20 h, the width is ~23 R_s, and at 40 h, the width increases to ~33 R_s. Thus, as the CME propagates into the heliosphere, it also expands in radial direction. We also notice that after the CME passed, the relative density behind the CME drops to negative (but the actual density remains positive), which is probably because the CME removes some of the background's mass when it propagates into the background solar wind.

From Figure 10, we find that the density changes very sharply at the CME's front edge, and we suppose that the shock front is located at the position with the maximum of the density gradient along the propagation direction in front of the CME. The blue dashed lines in Figure 11 show the time-height and the time-speed distribution of the shock front from the simulation. The green dash-dotted lines in Figure 11 give the height and the velocity of the shock front distribution deduced from the observations; to obtain the smooth distribution, we fit the observational data points in the shock drag model [*Vršnak et al.*, 2013; *Hess and Zhang*, 2014]. The red diamonds in Figure 11 mark the height and the velocity of shock front distribution from the harmonic mean (HM) triangulation [*Lugaz et al.*, 2010] based on the observations. From the comparison, we find that at the initial time within 6 h, the shock front deduced from simulation moves faster than that observed; then, the shock speed from simulation drops quickly and become similar to the observed shock speed. The fast shock may be caused by the large average speed of the plasma blob which was set to be 1494 km/s to fit the initial CME speed from the imaging data.

3.3. Comparisons With the Wind Data at 1 AU

Figure 12 depicts the plots of total x component, y component, and z component magnetic field (B_x, B_y, and B_z) at the GSE coordinate system; velocity; number density; and temperature at 1 AU, respectively, from the top to the bottom. Each panel describes the comparison of the simulated plasma parameters with the Wind-observed parameters. Figure 12 demonstrates that our data-constrained simulation can reproduce well some of the in situ measurements: the transit time of the shock about 48 h is approximately reproduced; the velocity, the total magnetic field, the temperature, and the density peak value are very close to the realistic values during the peak period. The leading shock, characterized by a sharp jump in the total magnetic field, B_x, B_y, and B_z; velocity; and temperature curves, arrive almost at the same time between the simulation and the in situ measurements.

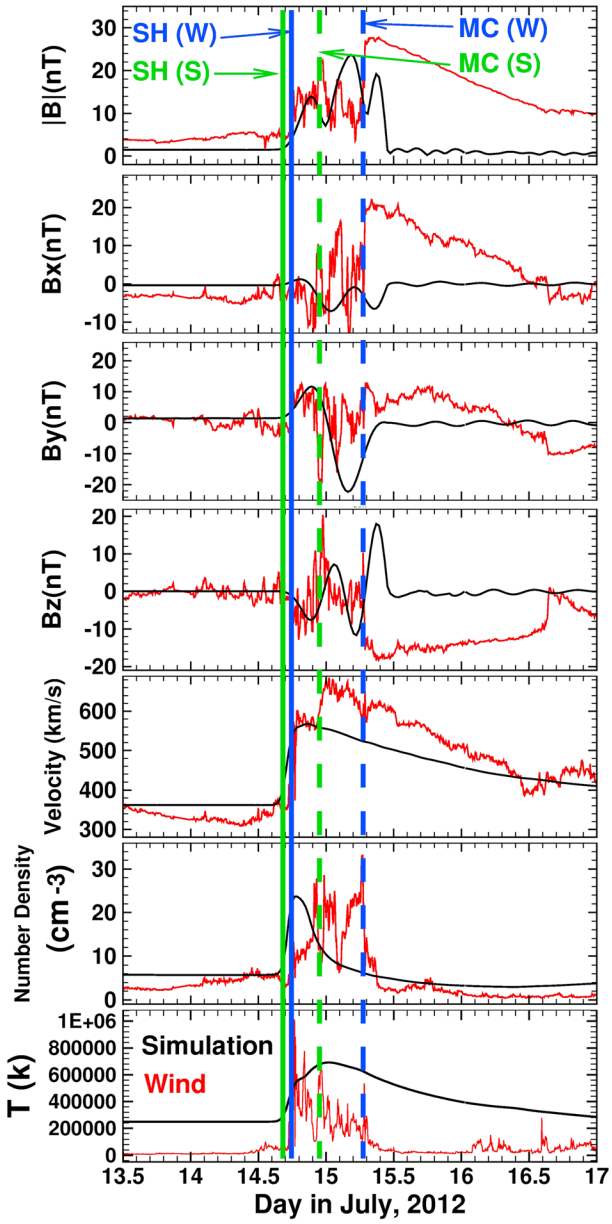

Figure 12. A comparison of the MHD simulation of the magnetic field and plasma parameters using the measured (Wind spacecraft) magnetic field and solar wind parameters at 1 AU. The black lines denote simulation parameters, and the red lines denote the measured parameters by Wind, (top to bottom) the magnetic field strength $|B|$ (nT), B_x (nT), B_y (nT), and B_z (nT) at the GSE coordinate system; the velocity (km/s); the proton density (cm^{-3}); and the proton temperature (K). The blue (or green) vertical solid lines indicate the arrival time at 1 AU of the shock, and the blue (or green) vertical dashed lines denote the arrival time of the magnetic cloud, from Wind data (or simulation).

Nevertheless, some quantitative disagreement is expected when compared simulation results with real observations. The blue vertical solid lines indicate the arrival time at 1 AU of the shock, and the blue vertical dashed lines denote the arrival time of the magnetic cloud, which was deduced from the in situ observations [*Möstl et al.*, 2014; *Hess and Zhang*, 2014]. The shock arrival is at 1 AU at 17:24 UT on 14 July, immediately followed by a sheath region. At about 06:00 UT on 15 July, the sheath region ended, and a magnetic cloud began [*Möstl et al.*, 2014]. The green vertical solid lines indicate the shock arrival time from the simulation, which is only ~1 h earlier than the observations.

The magnetic cloud in the simulation reaches 1 AU at about 22:30 UT on 14 July, marked by the green dashed lines, which is ~7.5 h earlier than the observed one. One reason about the disagreement is that the simulated flux rope size is not as large as the observed one. This is mainly caused by the limitation of the model, which assumes a magnetized plasma blob as the flux rope.

4. Summary and Discussion

We have investigated the evolution of the 12–16 June 2012 CME in a realistic ambient solar wind by using the 3-D data-constrained COIN-TVD MHD simulation. We first established a steady state background solar wind from the solar surface to the Earth's orbit (215 R_s) and beyond by using the observed line-of-sight magnetic field of CR 2125 on the photosphere. Our numerical results of the background solar wind show that the current sheet becomes nearly vertical to the ecliptic plane, which demonstrates the typical characteristics at solar maximum.

We simulated the CME by means of a high-density, high-velocity, and high-temperature magnetized plasma blob, which is superimposed on the background steady state solar wind. To reproduce the 12 July 2012 event, we chose the initial propagation direction and average velocity to be the same as those derived from the observations. The choice of other parameters is given to match the transit time of the shock, the total magnetic field, and other in situ data at the shock as the best fit as possible.

From the comparisons with remote sensing observations, the *J* map versus observations, as shown from Figures 5 to 10, we find that (1) we are able to reproduce successfully the observations in STA and STB fields of

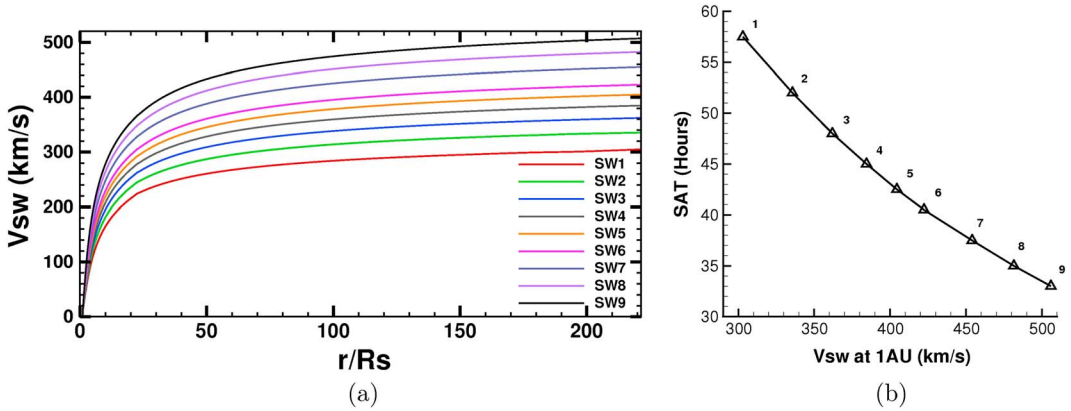

Figure 13. (a) Averaged background solar wind speed (V_{sw}) versus height in nine cases which is presented from SW1 to SW9. (b) Shock arrival time (SAT) in the nine cases versus V_{sw} at 1 AU.

view, for both the CME morphology and the CME kinematics and (2) our results for the shock front propagation are mainly consistent with the results from the shock drag model, except at the very early time.

When the CME evolves to ICME reaching 1 AU, its physical parameters (Figure 12) resemble the observations of the ICME recorded by the Wind spacecraft. Comparing our simulation results with the in situ data, we find that the transit time of the shock is approximately reproduced; the velocity, the total magnetic field, the temperature, and the density peak value are very close to the realistic values during the peak period. While there still exist some quantitative disagreements when compared simulation results with real observations, especially during the interval of a magnetic cloud. The possible reasons might be the uncertainty of the initial realistic solar wind speed and the IMF background conditions and uncertainty of the appropriate solar observations used to initiate the CME.

Besides, from studying the shock front speed-time distribution as shown in Figure 11, we find that at the initial time within 6 h, the shock front appears to decelerate very quickly from ~2300 km/s to ~1100 km/s; and at 6 h, the height of the shock front reaches up to ~56 R_s. Then from 56 R_s to 1 AU, the shock front decelerates slowly from ~1100 km/s to ~570 km/s. It has been found that the major force which caused the deceleration of a shock or CME is the aerodynamic drag force, $F_D = -\rho_e A C_D (V_i - V_e)|V_i - V_e|/\tau$, where τ and A are the volume and the cross-sectional area of the CME, C_D is the drag coefficient, V_i is the CME speed, and ρ_e and V_e are the density and speed of the background solar wind, respectively [*Cargill*, 2004; *Cargill et al*., 1994; *Schmidt and Cargill*, 2000; *Temmer et al*., 2012; *Shen et al*., 2012; *Vršnak and Gopalswamy*, 2002; *Owens and Cargill*, 2004; *Vršnak et al*., 2013]. Therefore, the choice of different solar wind speeds would affect the CME's transit time. Actually, *Heinemann* [2002] has also demonstrated that two major sources of uncertainty in the estimates of shock arrival times were the velocity and the density of the ambient medium.

In order to discuss the influence of the background solar wind speed on the shock arrival time (SAT) quantitatively, we have made a test by using the background solar wind with different speed through which the CME propagates. The average background solar wind speed (V_{sw}) against the heights in nine different cases is presented from SW1 to SW9 in Figure 13a. Then, the CME model which was described in section 2.2 is input into the different background solar wind. Figure 13b gives the SAT in the nines cases against V_{sw} at 1 AU. It could be found that the SAT is almost inversely proportional to the background solar wind. As the ambient solar wind speed at 1 AU increases from 300 km/s to 500 km/s, the transient time decreases from 57 h to 37 h. In other words, the slower the solar wind speed, the larger the aerodynamic drag force, the larger the deceleration of the CME, and thus the longer the transit time, which is consistent with the results by *Heinemann* [2002].

In summary, we have demonstrated that the data-constrained 3-D MHD simulation can reproduce the realistic observations to a large extent not only the arrival time but also the continuous kinematic process and morphological scenario structures from the Sun to the Earth. This study also reveals certain limitations of the numerical model, such as the less extension of the simulated flux rope. Further refinement of the numerical model is needed in order to fully simulate the observations.

Moreover, in our present numerical CME model, like many other numerical CME models, there exist two extremely important and still unsolved issues: the uncertainty of the initial realistic solar wind background conditions and the uncertainty of the appropriate solar observations used to "mimicking" solar flare/filament and CME initiation [*Dryer*, 1998; *Fry et al*., 2001; *Odstrcil et al*., 2004; *Shen et al*., 2007, 2011a, 2011b]. To some extent, our objective of using more observational data such as the photospheric magnetic fields by constraining the model is to try to reduce the uncertainty in the initial values of realistic solar wind. But it is still a challenging problem on how to use the approximate solar observations to initialize the solar flare/filament and CME.

Acknowledgments

The data for this work are available at the official websites of STEREO, SOHO, and Wind spacecraft. We acknowledge the use of them. STEREO is the third mission in NASA's Solar Terrestrial Probes program, and SOHO is a mission of international cooperation between ESA and NASA. The STEREO/SECCHI data are produced by a consortium of NRL (U.S.), LMSAL (U.S.), NASA/GSFC (U.S.), RAL (UK), UBHAM (UK), MPS (Germany), CSL (Belgium), IOTA (France), and IAS (France). The Wind data are obtained from the GSFC/SPDF OMNI Web interface at http://omniweb.gsfc.nasa.gov. The Wilcox Solar Observatory (WSO) data used in this study were obtained via the Web site http://wso.stanford.edu/synoptic.html for CR 2125. The WSO is currently supported by NASA. This work is jointly supported by grants from the 973 key projects (2012CB825601 and 2011CB811403), the Knowledge Innovation Program of the Chinese Academy of Sciences (KZZD-EW-01-4), the National Natural Science Foundation of China (41231068, 41174150, 41274192, 41131065, 41121003, 41274173, and 41474152), and the Specialized Research Fund for State Key Laboratories. J.Z. and P.H. are supported by NSF grants ATM-0748003 and AGS-1156120. We are very grateful to the two anonymous reviewers for their constructive and helpful comments.

Michael Liemohn thanks the reviewers for their assistance in evaluating this paper.

References

Baker, D. N., X. Li, A. Pulkkinen, C. M. Ngwira, M. L. Mays, A. B. Galvin, and K. D. C. Simunac (2013), A major solar eruptive event in July 2012: Defining extreme space weather scenarios, *Space Weather*, *11*, 585–591, doi:10.1002/swe.20097.

Cargill, P. J. (2004), On the aerodynamic drag force acting on interplanetary coronal mass ejections, *Sol. Phys.*, *221*, 135–149.

Cargill, P. J., J. Chen, and D. A. Garren (1994), Oscillations and evolution of curved current-carrying loops in the solar corona, *Astrophys. J.*, *423*, 854.

Chané, E., C. Jacobs, B. Van der Holst, S. Poedts, and D. Kimpe (2005), On the effect of the initial magnetic polarity and of the background wind on the evolution of CME shocks, *Astron. Astrophys.*, *432*, 331–339.

Chané, E., B. Van der Holst, C. Jacobs, S. Poedts, and D. Kimpe (2006), Inverse and normal coronal mass ejections: Evolution up to 1 AU, *Astron. Astrophys.*, *447*, 727–733.

Chané, E., S. Poedts, and B. Van der Holst (2008), On the effect of the initial magnetic polarity and of the background wind on the evolution of CME shocks, *Astron. Astrophys.*, *492*, L29–L32.

Chen, J., and J. Krall (2003), Acceleration of coronal mass ejections, *J. Geophys. Res.*, *108*(A11), 1410, doi:10.1029/2003JA009849.

Cheng, X., M. D. Ding, J. Zhang, X. D. Sun, Y. Guo, Y. M. Wang, B. Kliem, and Y. Y. Deng (2014), Formation of a double-deck magnetic flux rope in the sigmoidal solar active region 11520, *Astrophys. J.*, *789*, 93 pp., doi:10.1088/0004-637X/789/2/93.

Cohen, O., I. V. Sokolo, I. I. Roussev, N. Lugaz, W. B. I. Manchester, T. I. Gombosi, and C. N. Arge (2008), Validation of a global 3D heliospheric model with observations for the May 12, 1997 CME event, *J. Atmos. Sol. Terr. Phys.*, *70*, 583–592.

Davies, J. A., R. A. Harrison, A. P. Rouillard, N. R. Sheeley, C. H. Perry, D. Bewsher, C. J. Davis, C. J. Eyles, S. R. Crothers, and D. S. Brown (2009), A synoptic view of solar transient evolution in the inner heliosphere using the Heliospheric Imagers on STEREO, *Geophys. Res. Lett.*, *36*, 02102, doi:10.1029/2008GL036182.

Dryer, M. (1998), Multi-dimensional MHD simulation of solar-generated disturbances: Space weather forecasting of geomagnetic storms, *AIAA J.*, *36*(3), 365–370.

Dudík, J., M. Janvier, G. Aulanier, G. Del Zanna, M. Karlický, H. E. Mason, and B. Schmieder (2014), Slipping magnetic reconnection during an X-class solar flare observed by SDO/AIA, *Astrophys. J.*, *784*, 144.

Feng, X., S. T. Wu, F. Wei, and Q. Fan (2003), A class of TVD type combined numerical scheme for MHD equations with a survey about numerical methods in solar wind simulations, *Space Sci. Rev.*, *107*, 43–53.

Feng, X., C. Xiang, D. Zhong, and Q. Fan (2005), A comparative study on 3-D solar wind structure observed by Ulysses and MHD simulation, *Chin. Sci. Bull.*, *50*(7), 672–678.

Feng, X., L. P. Yang, C. Q. Xiang, S. T. Wu, Y. Zhou, and D. K. Zhong (2010), Three-dimensional solar wind modeling from the Sun to Earth by a SIP-CESE MHD model with a six-component grid, *Astrophys. J.*, *723*, 300–319.

Feng, X. S., S. H. Zhang, C. Q. Xiang, L. P. Yang, C. W. Jiang, and S. T. Wu (2011), A hybrid solar wind model of the CESE + HLL method with a yin-yang overset grid and an AMR grid, *Astrophys. J.*, *734*(1), 50, doi:10.1088/0004-637X/734/1/50.

Fry, C. D., W. Sun, C. S. Deehr, M. Dryer, Z. Smith, S.-I. Akasofu, M. Tokumaru, and M. Kojima (2001), Improvements to the HAF solar wind model for space weather predictions, *J. Geophys. Res.*, *106*, 20,985–21,002, doi:10.1029/2000JA000220.

Hayashi, K. (2005), Magnetohydrodynamic simulations of the solar corona and solar wind using a boundary treatment to limit solar wind mass flux, *Astrophys. J.*, *161*, 480–494.

Heinemann, M. (2002), Effects of solar wind inhomogeneities on transit times of interplanetary shock waves, *J. Atmos. Sol. Terr. Phys.*, *64*(3), 315–325.

Hess, P., and J. Zhang (2014), Stereoscopic study of the kinematic evolution of a coronal mass ejection and its driven shock from the Sun to the Earth and the prediction of their arrival times, *Astrophys. J.*, *792*, 49.

Howard, R. A., et al. (2008), Sun Earth Connection Coronal and Heliospheric Investigation (SECCHI), *Space Sci. Rev.*, *136*, 67–115.

Jackson, J. D. (1997), *Classical Electrodynamics*, 3rd ed., Wiley, New York.

Kaiser, M. L., T. A. Kucera, J. M. Davila, O. C. St. Cyr, M. Guhathakurta, and E. Christian (2008), The STEREO Mission: An introduction, *Space Sci. Rev.*, *136*, 5–16.

Levine, R. H., M. D. Altschuler, and J. W. Harvey (1977), Solar sources of the interplanetary magnetic field and solar wind, *J. Geophys. Res.*, *82*(7), 1061–1065, doi:10.1029/JA082i007p01061.

Lugaz, N., W. B. Manchester IV, and T. I. Gombosi (2005), The evolution of coronal mass ejection density structures, *Astrophys. J.*, *627*, 1019–1030.

Lugaz, N., W. B. Manchester, I. I. Roussev, G. Tóth, and T. I. Gombosi (2007), Numerical investigation of the homologous coronal mass ejection events from active region 9236, *Astrophys. J.*, *659*, 788–800.

Lugaz, N., A. Vourlidas, I. I. Roussev, and H. Morgan (2009), Solar-terrestrial simulation in the STEREO era: The January 24–25, 2007 eruptions, *Sol. Phys.*, *256*, 269–284.

Lugaz, N., J. N. Hernandez-Charpak, I. I. Roussev, C. J. Davis, A. Vourlidas, and J. A. Davies (2010), Determining the azimuthal properties of coronal mass ejections from multi-spacecraft remote-sensing observations with STEREO SECCHI, *Astrophys. J.*, *715*(1), 493–499.

Lugaz, N., C. Downs, K. Shibata, I. I. Roussev, A. Asai, and T. I. Gombosi (2011), Numerical investigation of a coronal mass ejection from an anemone active region: Reconnection and deflection of the 2005 August 22 eruption, *Astrophys. J.*, *738*, 127.

Manchester, W. B., T. I. Gombosi, I. Roussev, D. L. De Zeeuw, I. V. Sokolov, K. G. Powell, G. Tóth, and M. Opher (2004), Three-dimensional MHD simulation of a flux rope driven CME, *J. Geophys. Res.*, *109*, A01102, doi:10.1029/2002JA009672.

Manchester, W. B., A. Vourlidas, G. Tóth, N. Lugaz, I. I. Roussev, I. V. Sokolov, T. I. Gombosi, D. L. De Zeeuw, and M. Opher (2008), Three-dimensional MHD simulation of the 2003 October 28 coronal mass ejection: Comparison with LASCO coronagraph observations, *Astrophys. J.*, *684*, 1448.

Möstl, C., et al. (2014), Connecting speeds, directions and arrival times of 22 coronal mass ejections from the Sun to 1 AU, *Astrophys. J.*, *787*, 119.
Nakamizo, A., T. Tanaka, Y. Kubo, S. Kamei, H. Shimazu, and H. Shinagawa (2009), Development of the 3-D MHD model of the solar corona-solar wind combining system, *J. Geophys. Res.*, *114*, A07109, doi:10.1029/2008JA013844.
Ngwira, C. M., A. Pulkkinen, M. L. Mays, M. M. Kuznetsova, A. B. Galvin, K. Simunac, D. N. Baker, X. L. Li, Y. H. Zheng, and A. Glocer (2013), Simulation of the 23 July 2012 extreme space weather event: What if this extremely rare CME was Earth directed?, *Space Weather*, *11*, 671–679, doi:10.1002/2013SW000990.
Odstrcil, D., P. Riley, and X. P. Zhao (2004), Numerical simulation of the 12 May 1997 interplanetary CME event, *J. Geophys. Res.*, *109*, A02116, doi:10.1029/2003JA010135.
Odstrcil, D., V. J. Pizzo, and C. N. Arge (2005), Propagation of the 12 May 1997 interplanetary coronal mass ejection in an evolving solar wind structures, *J. Geophys. Res.*, *110*, A02106, doi:10.1029/2003JA010135.
Owens, M., and P. J. Cargill (2004), Predictions of the arrival time of coronal mass ejections at 1 AU: An analysis of the causes of errors, *Ann. Geophys.*, *22*, 661.
Rempel, M., M. Schüssler, and M. Knölker (2009), Radiative magnetohydrodynamic simulation of sunspot structure, *Astrophys. J.*, *691*(1), 640–649.
Riley, P., R. Lionello, Z. Mikić, and J. Linker (2008), Using global simulations to relate the three-part structure of coronal mass ejections to in situ signatures, *Astrophys. J.*, *672*, 1221.
Rouillard, A. P., et al. (2008), First imaging of corotating interaction regions using the STEREO spacecraft, *Geophys. Res. Lett.*, *35*, L10110, doi:10.1029/2008GL033767.
Russell, C. T., et al. (2013), The very unusual interplanetary coronal mass ejection of 2012 July 23: A blast wave mediated by solar energetic particles, *Astrophys. J.*, *770*, 38.
Schmidt, J. M., and P. J. Cargill (2000), A model for accelerated density enhancements emerging from coronal streamers in Large-Angle and Spectrometric Coronagraph observations, *J. Geophys. Res.*, *105*(A5), 10,455–10,464, doi:10.1029/1999JA900505.
Sheeley, N. R., Jr., et al. (1997), Measurements of flow speeds in the corona between 2 and 30 $R_{\odot}$, *Astrophys. J.*, *484*, 472.
Sheeley, N. R., Jr., et al. (2008), SECCHI observations of the Sun's garden-hose density spiral, *Astrophys. J. Lett.*, *674*, 109.
Shen, F., X. Feng, S. T. Wu, and C. Xiang (2007), Three-dimensional MHD simulation of CMEs in three-dimensional background solar wind with the self-consistent structure on the source surface as input: Numerical simulation of the January 1997 Sun-Earth connection event, *J. Geophys. Res.*, *112*, A06109, doi:10.1029/2006JA012164.
Shen, F., X. Feng, and W. B. Song (2009), An asynchronous and parallel time-marching method: Application to the three-dimensional MHD simulation of the solar wind, *Sci. chin. Ser. E: Technol. Sci.*, *52*(10), 2895–2902.
Shen, F., X. S. Feng, S. T. Wu, C. Q. Xiang, and W. B. Song (2011a), Three-dimensional MHD simulation of the evolution of the April 2000 CME event and its induced shocks using a magnetized plasma blob model, *J. Geophys. Res.*, *116*, A04102, doi:10.1029/2010JA015809.
Shen, F., X. S. Feng, Y. Wang, S. T. Wu, W. B. Song, J. P. Guo, and Y. F. Zhou (2011b), Three-dimensional MHD simulation of two coronal mass ejections' propagation and interaction using a successive magnetized plasma blobs model, *J. Geophys. Res.*, *116*, A09103, doi:10.1029/2011JA016584.
Shen, F., S. T. Wu, X. Feng, and C.-C. Wu (2012), Acceleration and deceleration of coronal mass ejections during propagation and interaction, *J. Geophys. Res.*, *117*, A11101, doi:10.1029/2012JA017776.
Shen, F., C. Shen, Y. Wang, X. Feng, and C. Xiang (2013), Could the collision of CMEs in the heliosphere be super-elastic? Validation through three-dimensional simulations, *Geophys. Res. Lett.*, *40*, 1457–1461, doi:10.1002/grl.50336.
Shen, C., Y. Wang, Z. Pan, B. Miao, P. Ye, and S. Wang (2014), Full halo coronal mass ejections: Arrival at the Earth, *J. Geophys. Res. Space Physics*, *119*, 5107–5116, doi:10.1002/2014JA020001.
Sun, W., C. S. Deehr, M. Dryer, C. D. Fry, Z. K. Smith, and S. I. Akasofu (2008), Simulated solar mass ejection imager and "Solar Terrestrial Relations Observatory-like" views of the solar wind following the solar flares of 27–29 May 2003, *Space Weather*, *6*, S03006, doi:10.1029/2006SW000298.
Temmer, M., et al. (2012), Characteristics of kinematics of a coronal mass ejection during the 2010 August 1 CME-CME interaction event, *Astrophys. J.*, *749*, 1.
Thernisien, A. F. R., R. A. Howard, and A. Vourlidas (2006), Modeling of flux rope coronal mass ejections, *Astrophys. J.*, *652*, 763.
Thernisien, A., A. Vourlidas, and R. A. Howard (2009), Forward modeling of coronal mass ejections using STEREO/SECCHI data, *Sol. Phys.*, *256*, 111–130.
Titov, V. S., Z. Mikic, J. A. Linker, and R. Lionello (2008), 1997 May 12 coronal mass ejection event: I. A simplified model of the pre-eruptive magnetic structure, *Astrophys. J.*, *675*, 1614.
Tóth, G., D. L. DeZeeuw, T. I. Gombosi, W. B. Manchester, A. J. Ridley, I. I. Roussev, and I. V. Sokolov (2007), Sun-to-thermosphere simulation of the 28–30 October 2003 storm with the space weather modeling framework, *Space Weather*, *5*, S06003, doi:10.1029/2006SW000272.
van der Holst, B., and R. Keppens (2007), Hybrid block-AMR in cartesian and curvilinear coordinates: MHD applications, *J. Comput. Phys.*, *226*, 925–946.
Vršnak, B., and N. Gopalswamy (2002), Influence of the aerodynamic drag on the motion of interplanetary ejecta, *J. Geophys. Res.*, *107*(A2), 1019, doi:10.1029/2001JA000120.
Vršnak, B., et al. (2013), Propagation of interplanetary coronal mass ejections: The drag-based model, *Sol. Phys.*, *285*, 295–315.
Wang, Y. M., P. Z. Ye, S. Wang, G. P. Zhou, and J. X. Wang (2002), A statistical study on the geoeffectiveness of Earth-directed coronal mass ejections from March 1997 to December 2000, *J. Geophys. Res.*, *107*(A11), 1340, doi:10.1029/2002JA009244.
Wu, S. T., and J. F. Wang (1987), Numerical tests of a modified full implicit Eulerian scheme with projected normal characteristic boundary conditions for MHD flows, *Comput. Methods Appl. Mech. Eng.*, *24*, 267–282.
Wu, S. T., A. H. Wang, Y. Liu, and J. T. Hoeksema (2006), Data driven magnetohydrodynamic model for active region evolution, *Astrophys. J.*, *652*, 800–811.
Wu, C.-C., Fry, C. D., Wu, S. T., Dryer, M., and Liou, K. (2007), Three-dimensional global simulation of interplanetary coronal mass ejection propagation from the Sun to the heliosphere: Solar event of 12 May 1997, *J. Geophys. Res.*, *112*, A09104, doi:10.1029/2006JA012211.
Yermolaev, Y. I., and M. Y. Yermolaev (2006), Statistic study on the geomagnetic storm effectiveness of solar and interplanetary events, *Adv. Space Res.*, *37*(6), 1175–1181.
Zhang, J., et al. (2007), Solar and interplanetary sources of major geomagnetic storms ($Dst \leq -100$ nT) during 1996–2005, *J. Geophys. Res.*, *112*, A10102, doi:10.1029/2007JA012321.
Zhou, Y. F., X. Feng, and S. T. Wu (2008), Numerical simulation of the 12 May 1997 CME event, *Chin. Phys. Lett.*, *25*, 790.
Zhou, Y. F., X. S. Feng, S. T. Wu, D. Du, F. Shen, and C. Q. Xiang (2012), Using a 3-D spherical plasmoid to interpret the Sun-to-Earth propagation of the 4 November 1997 coronal mass ejection event, *J. Geophys. Res.*, *114*, A07109, doi:10.1029/2008JA013844.